

The Photospheric Poynting Flux and Coronal Heating

B. T. WELSCH

Space Sciences Laboratory, UC, Berkeley

welsch@ssl.berkeley.edu

(Received ; accepted)

Abstract

Some models of coronal heating suppose that random (cf., coherent) convective motions at the photosphere shuffle the footpoints of coronal magnetic fields and thereby inject sufficient magnetic energy upward to account for observed coronal and chromospheric energy losses in active regions. Using high-resolution observations of plage magnetic fields made with the Solar Optical Telescope aboard the *Hinode* satellite, we observationally test this idea by estimating the upward transport of magnetic energy — the vertical Poynting flux, S_z — across the photosphere in a plage region. To do so, we combine: (i) estimates of photospheric horizontal velocities, \mathbf{v}_h , determined by local correlation tracking applied to a sequence of line-of-sight magnetic field maps from the Narrowband Filter Imager, with (ii) a vector magnetic field measurement from the SpectroPolarimeter. Plage fields are ideal observational targets for estimating energy injection by convection, because they are: (i) strong enough to be measured with relatively small uncertainties; (ii) not so strong that convection is heavily suppressed (as within umbrae); and (iii) unipolar, so S_z in plage is not influenced by mixed-polarity processes (e.g., flux emergence) that cannot explain steady heating in stable, active-region fields. In this and a previously analyzed plage region, we found that the average S_z varied between the regions, but was positive (upward) and sufficient to explain coronal heating, with values near 2×10^7 erg cm⁻² s⁻¹. We find the energy input per unit magnetic flux to be on the order of 10^4 erg s⁻¹ Mx⁻¹. A comparison of intensity in a Ca II image co-registered with one plage magnetogram shows stronger spatial correlation with unsigned vertical field, $|B_z|$, than either S_z or horizontal flux density, B_h .

Key words: Magnetic Fields — Sun:photosphere — Sun:corona

1. Introduction

How is the solar corona heated to temperatures of ~ 1 MK, when the lower layers of the solar atmosphere are $\sim 10^4$ K or less? Evidently, the energy needed to heat the Sun's

atmosphere must cross the photosphere in some organized form before being converted into heat (disorganized, “thermalized” energy) in the chromosphere and corona. Because the magnetic fields that permeate the corona are all anchored at the photosphere, they are natural candidates for energetic coupling between the solar interior and corona. In the interior, motions in the Sun’s gas are driven by convection, and some fraction of the kinetic energy in turbulent convective motions is thought to be converted into energy stored in magnetic fields that is later dissipated as heat. To be a viable coronal heating mechanism, the input energy must be commensurate with observed energy losses in active region (AR) fields, estimated by Withbroe & Noyes (1977) to be $\sim 1 \times 10^7$ erg cm $^{-2}$ sec $^{-1}$ for the corona and $\sim 2 \times 10^7$ erg cm $^{-2}$ sec $^{-1}$ for the chromosphere. Waves were thought once thought to be primarily responsible for coronal and chromospheric heating (see, e.g., Withbroe and Noyes 1977). While waves (e.g., Tomczyk et al. 2007) and wave dissipation (e.g., Hahn et al. 2012) have been reported in the corona, currently available observations have not demonstrated that they supply sufficient energy to heat the active-region corona. Other models posit that random (cf., coherent) convectively-driven motions could inject sufficient magnetic energy, which is the primary hypothesis that we explore here.

There is a long history of modeling this convection-driven coronal energy input. Parker (1983a, 1983b) proposed that convection braids and twists the photospheric footpoints of coronal magnetic fields, and thereby injects energy into the corona. This energy is stored in current sheets, and is transiently dissipated in small bursts referred to as nanoflares (Parker 1988), with typical energies of $\sim 10^{24}$ erg, about 10^{-9} of the energies in very large flares. Galsgaard & Nordlund (1996) modeled an idealization of this process by imposing shearing flows on the upper and lower boundaries of an initially uniform field in an MHD simulation, and found sufficient power to heat the corona. Gudiksen & Nordlund (2002) imposed a more complex flow field, meant to mimic convective motions, on an MHD model of the coronal field and also found sufficient power, as well as morphology consistent with aspects of coronal observations. In the framework of reduced MHD, Rappazzo et al. (2008), also found sufficient power, even though fields in their model were only weakly braided. More recently, Bingert & Peter (2011) also modeled this process in MHD with a detailed treatment of the energy equation and found heating that is transient in time and space, and concentrated in and near the modeled transition region.

One promising observational approach to constraining models of coronal heating is to analyze time evolution of magnetic fields at the photosphere, where the magnetic field is precisely and routinely measured. Clear evidence of braiding or twisting motions would support the mechanism proposed by Parker. Schrijver et al. (1998) proposed that continuous emergence and cancellation of small-scale fields in the quiet Sun’s “magnetic carpet” leads to reconnection and heating, but Close et al. (2004) used sequential potential models of quiet-Sun fields to argue that emergence and cancellation are not required: just reconnection between existing flux systems, as their photospheric footpoints move, should be sufficient. Meyer et al. (2013) recently

directly incorporated magnetogram sequences into the lower boundary of a magnetofrictional model of quiet-sun coronal field evolution.

Yeates et al. (2014) recently investigated analytic expressions for lower bounds on the upward-directed Poynting flux of magnetic energy in a region of plage fields in NOAA AR 10930, based upon observed photospheric magnetic and velocity fields. The flows they analyzed were estimated by Welsch et al. (2012), who applied Fourier Local Correlation Tracking (FLCT; Fisher and Welsch 2008) to a sequence of line-of-sight magnetograms (magnetic field maps) of this active region. These “line-wing” magnetograms were observed with the Narrowband Filter Imager (NFI) instrument on the Solar Optical Telescope (SOT) (Tsuneta et al. 2008; Suematsu et al. 2008; Ichimoto et al. 2008; Shimizu et al. 2008) aboard the *Hinode* satellite (Kosugi et al. 2007), with a cadence $\simeq 120$ s, over about 13 hours on 2006 December 12 – 13.

Yeates et al. (2014) compared their lower bounds on the Poynting flux with a direct estimate of the Poynting flux, obtained with a procedure that we explain in detail here. First, they assumed that photospheric magnetic field, \mathbf{B} , is frozen to the plasma — a valid assumption in quite general circumstances (see, e.g., Parker 1984). Then the photospheric electric field, \mathbf{E} , is well approximated by $-(\mathbf{v} \times \mathbf{B})/c$, where \mathbf{v} is the photospheric velocity. Then the (vector) Poynting flux of magnetic energy, \mathbf{S} , can be expressed in terms of \mathbf{v} and \mathbf{B} as

$$\mathbf{S} = \mathbf{B} \times (\mathbf{v} \times \mathbf{B})/4\pi . \quad (1)$$

Approximating the photospheric surface as locally planar, we adopt Cartesian geometry, and use z and h to refer to vertical and horizontal directions, respectively. Then the vertical component of the Poynting flux is

$$S_z = [v_z B_h^2 - (\mathbf{v}_h \cdot \mathbf{B}_h) B_z]/4\pi . \quad (2)$$

This expression for total Poynting flux has been conceptually divided into an “emergence” term, which contains v_z , and a “shear” term, which contains \mathbf{v}_h (Liu & Schuck 2012; Parnell & De Moortel 2012). In fact, both terms involve the emergence of magnetized plasma across the photosphere. Since Yeates et al. (2014) were primarily focused on heating in plage — regions of nearly-vertical field when new flux is not emerging — the shearing term should dominate, meaning

$$S_z^{\text{plage}} \simeq -(\mathbf{v}_h \cdot \mathbf{B}_h) B_z/4\pi . \quad (3)$$

Yeates et al. (2014) treated the flows estimated by FLCT as horizontal velocities. We note that there is some controversy about how to interpret of velocities determined by correlation tracking and other “optical flow” (Schuck 2006) methods. Démoulin & Berger (2003) suggested that the apparently horizontal flows estimated by LCT are a linear combination of the horizontal velocity with the vertical velocity, with weighting determined by the ratio of horizontal to vertical field. Schuck (2008), however, used synthetic magnetograms extracted from MHD simulations, in which the true flows are known, to show that optical flow methods

essentially estimate the horizontal velocity, \mathbf{v}_h , although these estimates can be affected by vertical flows.

The NFI line-wing magnetograms only provide estimates of the line-of-sight (LOS) field, B_{LOS} , but the expressions for the Poynting flux given above all require knowledge of the vector magnetic field, \mathbf{B} . Accordingly, Yeates et al. (2014) co-registered the (12 Mm \times 12 Mm) region of the NFI field of view (FOV) that they studied with the corresponding sub-region of a vector magnetogram observed by SOT’s SpectroPolarimeter (SP; Tsuneta et al. 2008). This vector magnetogram was prepared by Schrijver et al. (2008) and is available online. The co-alignment procedure followed the approach used by Welsch et al. (2012), described in their Appendix.

By combining \mathbf{v}_h estimated with FLCT with \mathbf{B} from the SP magnetogram, Yeates et al. (2014) estimated the average Poynting flux to be 1.3×10^7 erg cm $^{-2}$ s $^{-1}$. This energy flux is sufficient to power coronal heating, but cannot fully satisfy chromospheric energy demand in active regions. Insufficient Poynting flux would indicate that processes on spatial or temporal scales that are unresolved in these photospheric observations (e.g., waves or smaller-scale footpoint shuffling) play a significant role in heating.

Despite the central role of the Poynting flux in theories of coronal heating, to our knowledge, no observational estimates of Poynting flux in the context of coronal heating have been published prior to the work by Yeates et al. (2014). How typical is the value they report? How is the Poynting flux related to magnetic field structure?

To address these and other questions, we report here an additional estimate of the Poynting flux from another plage region in the same active region, and investigate the properties of this energy flux. The remainder of this paper is organized as follows. In the next section, we briefly describe the magnetic field data and tracking methods we used to estimate \mathbf{v}_h . In Section 3, we first present our estimates of the Poynting flux in two plage regions of AR 10930, then analyze the Poynting fluxes’ correlations with magnetic structure in the region. The region of the NFI FOV that we analyze here was also observed in Ca II by SOT’s Broadband Filter Imager (BFI; Tsuneta et al. 2008), and in §3.3 we compare this chromospheric emission with the spatial distributions of Poynting flux and magnetic field components. Finally, we conclude with a brief discussion of our results in Section 4.

2. Data & Methods

2.1. NFI Magnetograms

Many aspects of the NFI magnetograms that we track to estimate \mathbf{v}_h are described by Welsch et al. (2012). These Fe I 6302 Å (shuttered) magnetograms of AR 10930 have 0.16'' pixels, and were created from the Stokes V/I ratio in Level 0 data. The data were recorded between 12-Dec-2006 at 14:00 and 13-Dec-2006 at 02:58, with a cadence of 121.4 ± 1.2 s, except for three gaps of 10 minutes and two relatively small time steps of 26 s each. The

USAF/NOAA Solar Region Summary issued at 24:00 UT on 12-Dec-2006 listed AR 10930 at S06W21, meaning it was relatively near disk center during the interval we study. Since the diffraction limit of SOT is near $0.32''$, we rebinned the magnetograms (2×2). During this era of the *Hinode* mission, a bubble present within the NFI instrument degraded image quality in the upper part of the NFI field of view; we ignore pixels from this region in our analyses.

We converted the measured Stokes I and V signals into pixel-averaged flux densities, which we denote B_{NFI} , using the approximate calibration employed by Isobe et al. (2007). While the linear scaling in this approach breaks down in umbrae, it should not be problematic for plage regions. Note that we use evolution in image structure in the NFI magnetograms to derive velocities, but do not use the estimated flux densities directly in any calculations; for correlation tracking, what matters is that the images capture the *spatial structure* of magnetic fields at each time in the sequence. Welsch et al. (2012) estimated the NFI noise level following Hagenaar et al. (1999), by fitting the core of the distribution of flux densities ($\pm 10 \text{ Mx cm}^{-2}$) in each frame with a Gaussian. Based upon these fits, they adopted a uniform uncertainty estimate of $\pm 15 \text{ Mx cm}^{-2}$ for B_{NFI} over the 13-hour run.

Prior to tracking these magnetograms, Welsch et al. (2012) co-aligned them in time to remove spacecraft jitter and jumps from pointing changes. Spectral analysis showed some power at the orbital frequency, but no clear evidence of helioseismic p-mode leakage into the estimated magnetic flux densities.

2.2. SP Vector Magnetograms

As mentioned above, Schrijver et al. (2008) used SP data to estimate the vector magnetic field in AR 10930, and one of the two vector magnetograms they analyzed falls within our tracking interval, around 21:00 UT. The SP scan ran from 20:30 - 21:15, with $\sim 0.3''$ pixels. For this study, we analyzed two versions of this magnetogram. In the first version, the field was derived as described by Schrijver et al. (2008), but was not reprojected. We refer to this plane-of-sky (POS) SP magnetogram as the POSSP magnetogram. In the second version, the data were reprojected to represent the field on a Cartesian plane, and the data mapped onto a grid with a pixel scale of approximately $0.63''$ per pixel. (This was done to reduce the array size for computational expediency in extrapolating coronal fields.) We will refer to this reduced-resolution SP magnetogram as the RRSP magnetogram. (The RRSP magnetogram produced by Schrijver et al. (2008) is online, in FITS format, at <http://www.lmsal.com/~schryver/NLFFF/>; file contents are described in the FITS header comment field.) As discussed below, our results for the Poynting flux are very similar for both versions of this magnetogram, demonstrating that minor changes in data handling (e.g., interpolations) do not introduce large uncertainties in our results.

For the POSSP data, we adopt a locally Cartesian reference frame, and refer to the radial field as B_z , the azimuthal field as B_x , and $-B_\theta$ as B_y . While this is somewhat inaccurate over

SP, 2006/12/12, c.20:50; NFI contours

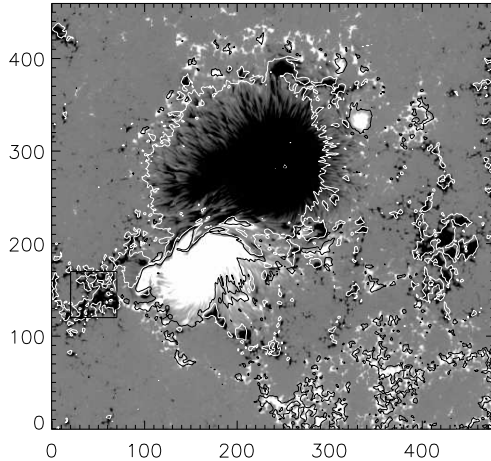


Fig. 1. Grayscale: B_z from the POSSP data (saturation at ± 750 G), with ± 250 Mx cm^{-2} contours of B_{NFI} overplotted (black for flux toward the observer, white for away). The plage region that is the focus of our study in the black box at lower left. Rastering for the SP observation was left-to-right, and the observing duration was much longer for the SP data than for the NFI data, leading to some local discrepancies between the fields.

the FOV of the whole active region, it is not problematic in the (51×51) pixel² area of plage that we study (about one heliocentric degree on a side). Figure 1 shows B_z from the POSSP data in grayscale, with ± 250 Mx cm^{-2} contours of B_{NFI} overplotted (black for flux toward the observer, white for away). The plage region that is the focus of our study in the black box at lower left. In this image, the x coordinates for contours of B_{NFI} were stretched by 1.01 from the SP data, necessary to account for a small discrepancy between the $0.32''$ NFI pixels versus the data interpolated from $\sim 0.3''$ SP raster steps. Rastering for the SP observation was left-to-right, and the observing duration was much longer for the SP data than for the NFI data, leading to some local discrepancies between the fields. The scan across our plage region took about three minutes, near the start of the sequence.

Welsch et al. (2012) described large-scale alignment of the RRSP magnetogram with the NFI field in detail. In their Figure 20, comparing panels (a) and (b) (or panels (b) and (d) in Fig. 1 of Schrijver et al. 2008) reveals some stretching — primarily horizontal — of the morphology of AR 10930 in the SP data. Given the position of AR 10930 near S06W21, foreshortening is too small to account for the magnitude of this distortion, with about 300 RRSP pixels covering the same horizontal distance as 250 NFI pixels — a discrepancy of 20%. Welsch et al. (2012) and Yeates et al. (2014) therefore used repeated Fourier interpolations to spatially interpolate the RRSP data onto each column of the $0.32''$ NFI grid (thereby oversampling the $0.63''$ RRSP pixels), an approach we also used here. In the process, we reduced the horizontal extent of RRSP pixels by 5%, chosen to maximize agreement between B_{NFI} and B_z from the SP data in

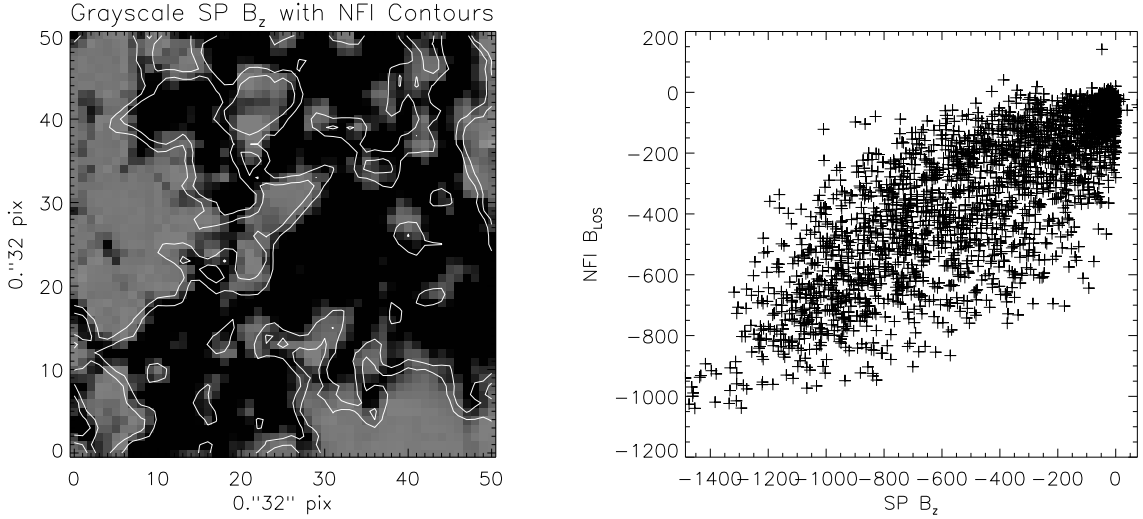


Fig. 2. Left: Contours of B_{NFI} at -125 and -250 Mx cm^{-2} over a grayscale image of B_z from the POSSP data (saturation set to $\pm 500 \text{ G}$) in the plage region in the left panel of Figure 1. Right: a scatter plot of B_z from the POSSP data versus B_{NFI} . The rank-order and linear correlation coefficients are both 0.82.

the plage region that we analyze here. (Welsch et al. [2012] found the stretching across the full FOV to be non-uniform, as would be expected for reprojection, but it appears locally linear in the horizontal direction.) Note that distortion by foreshortening in our plage region (17° from disk center) should be a 5% effect, and nearly uniform across the region.

The plage region that we studied is a (51×51) pixel² area in the data with $0.32''$ pixels. In the (2×2) -binned NFI data, this corresponds to $x \in [32, 82]$ and $y \in [140, 190]$. We roughly co-aligned the SP data by hand to within a few pixels, and then computed the cross-correlation of the nearly-aligned images to find the whole-pixel shift at the maximum of the cross-correlation function. Residual shifts for the POSSP and RRSP data in (x, y) are $(-0.03, 0.38)$ and $(-0.04, 0.03)$ pixels, respectively. To illustrate the co-alignment, we plot contours of B_{NFI} at ± 125 and $\pm 250 \text{ Mx cm}^{-2}$ over a grayscale image of B_z from the POSSP data in the plage region in the left panel of Figure 2. In the right panel, we show a scatter plot of B_z from SP versus B_{NFI} . The rank-order and linear correlation coefficients are both 0.82. A fit of B_{NFI} to B_z from the POSSP data yields a slope near 0.6, implying weaker flux densities for B_{NFI} . (The POSSP data incorporates a filling factor estimate.) Discrepancies probably arise primarily from both the more accurate polarimetric inversion of the SP data and evolution in the fields while the SP was rastered.

The mean and median vertical fields in this region are -434 G and -354 G , respectively. The mean unsigned B_z has the same magnitude as mean B_z , so the region really is unipolar. The mean and median horizontal field strengths are 160 G and 121 G , respectively, and the mean and median inclination angles are 154° and 157° , respectively — so 26° and 23° from vertical.

Deriving error estimates for the vector field is not straightforward. We examined the histogram of line-of-sight field strengths over the full (931×512)-pixel SP FOV, but found the core exhibits an unexpected dearth of field values within about ± 5 G of zero, so fitting the core would not be meaningful. Nonetheless, the shape of the histogram within ± 20 G suggests that the FWHM of the distribution would be about 20 G; this is also the median unsigned line-of-sight field strength. This value might more accurately represent intrinsic variability in the line-of-sight field than measurement error, but we expect it is a good upper limit on the noise level in the line-of-sight field. Given the relatively strong vertical fields in our near-disk-center plage region, the fractional error in B_z is therefore likely to be small — about 5%. For the horizontal fields, the situation is less clear. The median transverse field strength over the whole FOV is only 8 G, and the FWHM of the histogram of transverse field values is about only 5 G. Almost exactly 1/3 of pixels have a transverse field stronger than 30 G; we suggest this is a good “1- σ ” level, since 2/3 of the distribution falls below it. This transverse-field uncertainty would imply fractional errors in horizontal fields in our plage region of about 25%. If errors in B_z and \mathbf{B}_h were uncorrelated, then their combined impact on the Poynting flux would be negligible. Both the inversion process used to derive \mathbf{B} and the reprojection of the magnetic vector from LOS/POS components into vertical/horizontal components, however, imply the errors are coupled. Nonetheless, we expect the impact of measurement errors in \mathbf{B} on S_z^{plage} to be relatively small in all summed results: since all the quantities that are summed are signed (from the product of B_z with the dot product of \mathbf{B}_h with \mathbf{v}_h), some cancellation should occur.

2.3. Tracking the NFI Magnetograms

Many tracking algorithms estimate spatial displacements of local structures in a pair of images separated in time by an interval Δt . Tracking methods then typically have at least two free parameters: the size L of the local neighborhood (around each pixel for which a velocity is sought) in which structures between the two images are associated; and the time interval Δt between images. Accordingly, we briefly discuss our tracking parameters.

In some cases, Δt is tightly constrained by the cadence of observations. If, however, cadences are relatively rapid compared to the expected time scale of evolution of image structures, then successive images are likely to differ only by the noise in each measurement (Welsch et al. 2012). Consequently, using the highest possible cadence for a given sequence of observations might be unwise. Welsch et al. (2012) suggested that temporal stability in the reconstructed flow maps provides a useful constraint in determining the optimal Δt : two flow fields estimated at times t_1 and t_2 (from images pairs at $\{t_1 - \Delta t/2, t_1 + \Delta t/2\}$ and $\{t_2 - \Delta t/2, t_2 + \Delta t/2\}$, respectively) should be very similar if $|t_2 - t_1|$ is shorter than the time scale of evolution in the flow field. In the NFI dataset, Welsch et al. (2012) found that successive flow maps were poorly correlated at the observing cadence ($\simeq 120$ s), so Δt should be larger. They also found worse agreement between successive flow maps estimated without first temporally averaging the input

magnetograms. Accordingly, the flows we analyze here were derived with $\Delta t = 8$ min, and the initial and final magnetograms were computed by applying a five-step boxcar average to the NFI magnetograms.

As noted above, the size L of the localization (or “apodization window” or “aperture”) function applied to the input images prior to tracking is set by the user. Typical weighting functions are Gaussians or “top-hats” centered on each pixel for which a velocity estimate is sought. In FLCT, L is set via the σ parameter in FLCT’s weighting function, $\propto \exp(-r^2/\sigma^2)$, where r is the horizontal distance (in pixels) from each pixel for which a velocity is sought.

The best procedure to select an optimal L is unclear. As noted by Welsch et al. (2004), the estimated velocity can be used to reconstruct the observed evolution between the images; and as noted by Welsch et al. (2007) and Schuck (2008), the windowing parameter can be chosen to optimize consistency of this reconstruction with observations. A perfectly consistent reconstruction (see, e.g., Welsch et al. 2011), however, is undesirable: exact matching of observations is problematic because any noise or artifacts in the input images is propagated directly into the estimated electric fields (Schuck 2006). Welsch et al. (2012) also noted that a given choice of L implies averaging over dynamics on spatial scales smaller than L . To fully exploit the spatial resolution of SOT, therefore, a smaller L would be better. Schuck (2006) noted, however, that, in the presence of noise, information from several pixels is essential to prevent spurious fluctuations from noise from obscuring actual physical displacements. Consequently, selecting too small an L can increase susceptibility to noise, since not enough pixels are used in estimating each local displacement. Indeed, Welsch et al. (2012) found that relatively small σ ’s resulted in low correlations between successive flow maps, suggesting the influence of fluctuations from noise. Accordingly, we analyze flow maps derived with $\sigma = 4$ pixels here, which balances preservation of spatial resolution with the need for significant frame-to-frame correlations in flows, to ensure robustness in our estimates.

We also attempt to minimize confusion of fluctuations due to noise in the input magnetograms with *bona fide* magnetic evolution by not estimating velocities in pixels below the noise level. Accordingly, pixels with unsigned flux densities below the 15 Mx cm^{-2} noise level for the NFI images estimated by Welsch et al. (2012) were not tracked.

In Figure 3, we plot both horizontal magnetic field vectors and FLCT flow vectors over a grayscale image of B_z , for the flow map centered at 20:30:20 UT. Velocities tend to be larger in field-free regions, consistent with the general tendency of strong vertical fields to suppress convection (Title et al. 1992; Berger et al. 1998; Bercik 2002; Welsch et al. 2009; Welsch et al. 2012). The mean and median horizontal FLCT velocities, among pixels where estimates were made, are 0.15 km s^{-1} and 0.12 km s^{-1} , respectively.

In addition, as a check upon our results, we have tracked the NFI data with a separate LCT code, one provided by Y.-J. Moon (private communication) that has been used in other published work (e.g., Moon et al. 2002). While FLCT computes the cross-correlation function

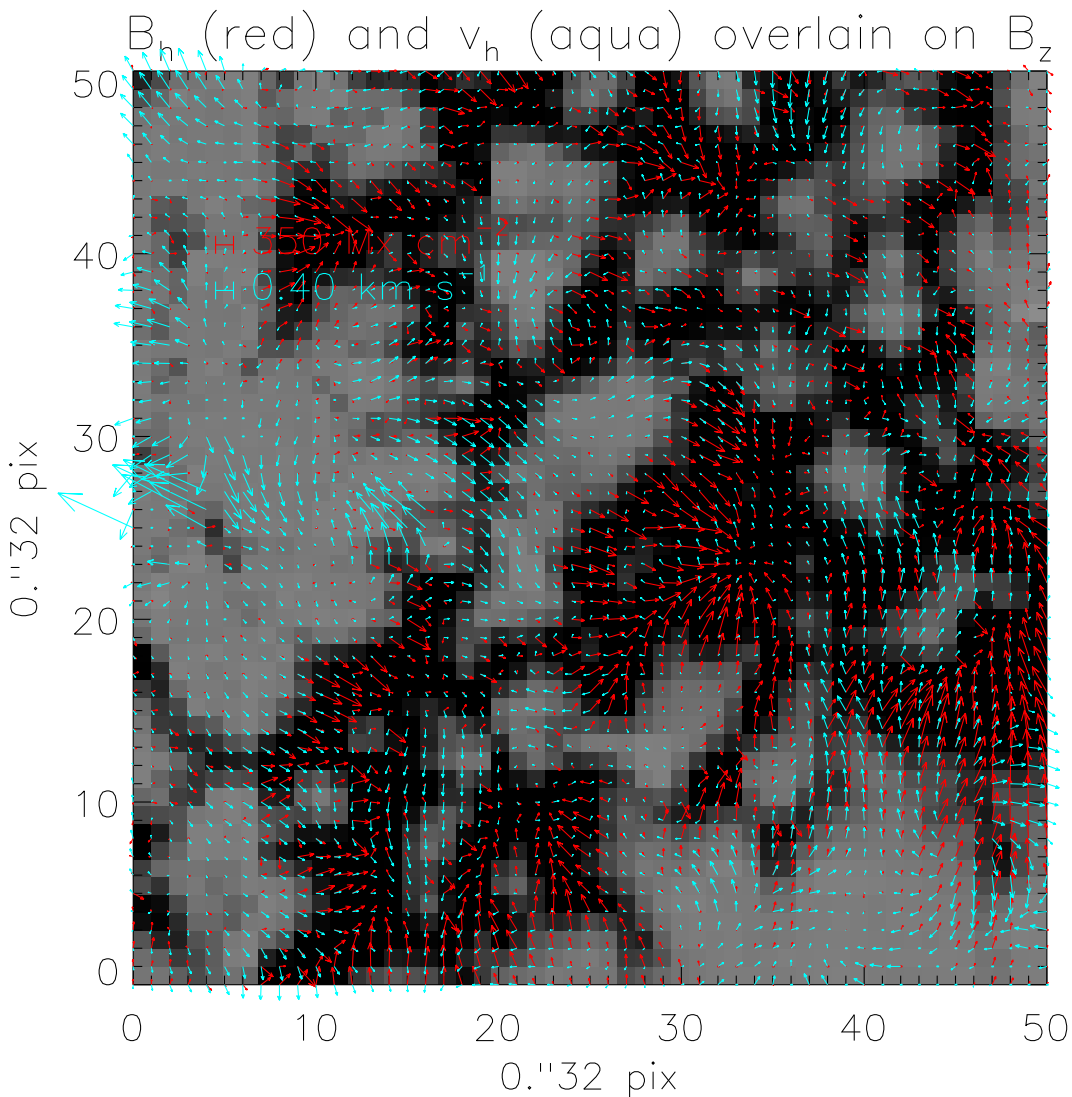


Fig. 3. Horizontal magnetic field (red) and FLCT velocities (aqua) overlotted on a grayscale image of B_z (saturation at ± 750 G) from the POSSP magnetogram.

in Fourier space, this second tracking code computes the correlation function in regular space, following November & Simon (1988). Hence, we refer to it as Spatial LCT (SLCT), in contrast to Fourier LCT. We also only tracked pixels with absolute flux density above 15 Mx cm^{-2} , with the same Δt , but set σ in this code to 3 pixels, since its weighting function includes a factor of 2 in the denominator of the exponential, $\propto \exp(-r^2/2\sigma^2)$. This routine returned either excessively large velocities in some pixels or even NaNs (in 4% of tracked pixels). Velocities in excess of 5 km s^{-1} ($< 0.4\%$ of tracked pixels) or equal to NaN were set to zero.

In the left panel of Figure 4, we show SLCT velocities overlain on B_z from the POSSP data. Comparison of these flows with those in Figure 3 shows rough agreement in many places, but also clear disagreements in others. Rank-order correlation coefficients between these methods' v_x and v_y estimates are 0.68 and 0.73, respectively. Consistent with this significant

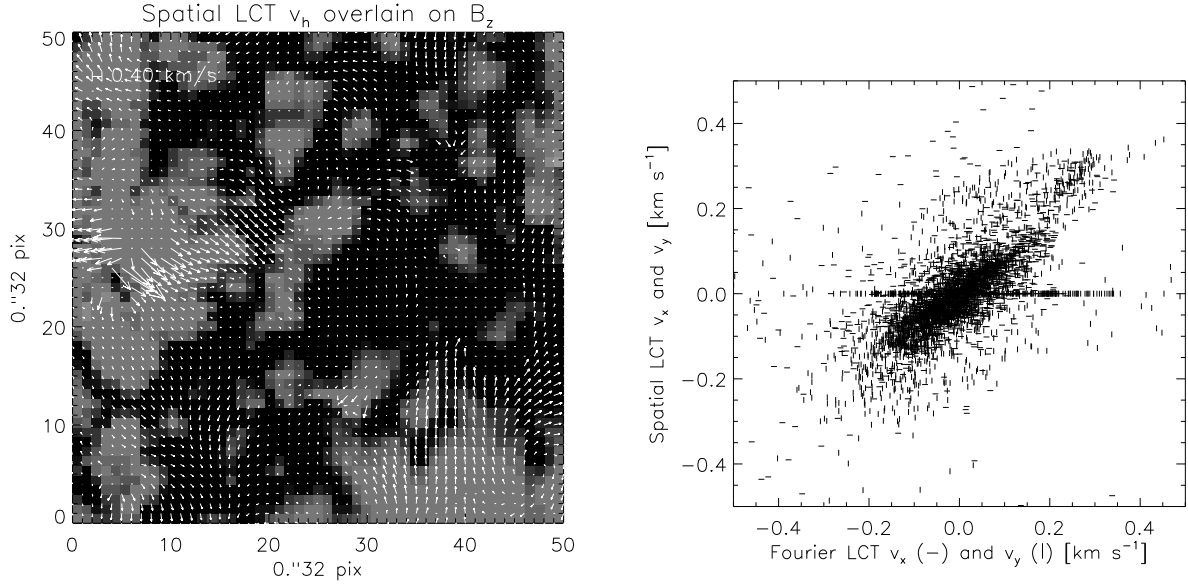


Fig. 4. Left: SLCT velocity vectors overlotted on a grayscale image of B_z (saturation at ± 500 G) from the POSSP magnetogram. Right: A scatter plot comparing v_x (—'s) and v_y (|'s) from FLCT and SLCT.

correlation, a scatter plot in the right panel of Figure 4 shows that the flows are substantially correlated. The mean and median horizontal SLCT velocities, among pixels where estimates were made, are 0.13 km s^{-1} and 0.10 km s^{-1} , respectively, quite close to the values for FLCT.

3. Results

3.1. Poynting Fluxes

We combined the FLCT flows estimated from the NFI data with the co-registered vector magnetic field from SP in equation (3) to compute the Poynting flux averaged over the plage region. Using the POSSP data, we find a net positive average Poynting flux, $S_z^{\text{plage, FLCT}} = 2.19 \times 10^7 \text{ erg cm}^{-2} \text{ s}^{-1}$, very similar to the $2.20 \times 10^7 \text{ erg cm}^{-2} \text{ s}^{-1}$ that we get using the RRSP data. The similar POSSP / RRSP values demonstrate that different interpolations of the SP data are not a significant source of error (perhaps unsurprising). In Figure 5, we show a grayscale map of the Poynting flux, with saturation set to $\pm 7 \times 10^8 \text{ erg cm}^{-2} \text{ s}^{-1}$, overlain with -125 G and -250 G contours of B_z from the POSSP data. Regions with both positive and negative Poynting flux are visible, but the net Poynting flux is positive. Using the SLCT flows with the POSSP data, we also find a net positive Poynting flux, but estimate $S_z^{\text{plage, SLCT}} = 2.48 \times 10^7 \text{ erg cm}^{-2} \text{ s}^{-1}$, about 13% larger than the FLCT result. The Poynting flux maps are significantly correlated, with a pixel-wise rank-order correlation of 0.58. Our simplistic estimate of uncertainties in the magnetic field (§2.2 above) suggests that fractional errors in \mathbf{B} could be smaller, but are probably commensurate. Evidently, the flow estimation process is a source of at least a $\sim 15\%$ uncertainty in our estimates. Further study of this same

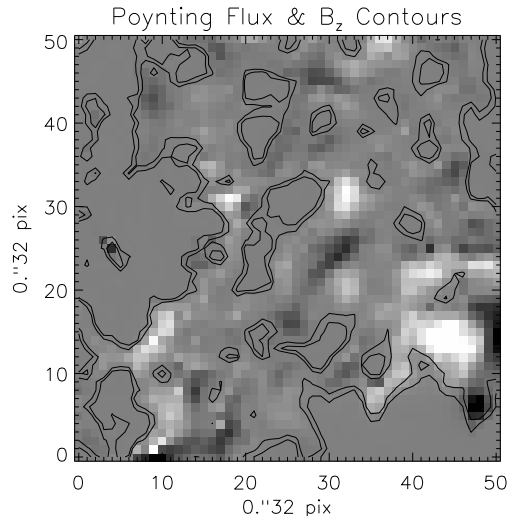


Fig. 5. The grayscale map shows the Poynting flux, with saturation set to $\pm 7 \times 10^8 \text{ erg cm}^{-2} \text{ s}^{-1}$, overlain with -125 G and -250 G contours of B_z from the POSSP data. Regions with both positive and negative Poynting flux are visible, but the net Poynting flux is positive.

data set, using a different tracking method (e.g., DAVE or DAVE4VM; Schuck 2006, Schuck 2008) would be worthwhile.

It is not surprising that different flow methods yield somewhat different results. Welsch et al. (2007) compared flows estimated by several methods using synthetic magnetograms extracted from MHD simulations of an emerging magnetic flux tube in the solar interior, in which the true velocities were known. Flows from most of the methods were significantly correlated with both each other and with the true flows. But flows from the various methods did not agree closely, and most of the methods only recovered a fraction of the Poynting flux. Results from the tests by Welsch et al. (2007), however, are probably not applicable here, because the rising-flux-tube magnetic geometry in the MHD data they used is very different than our plage region: their field was primarily horizontal, and the Poynting flux was dominated by the emergence term, not the shearing term. For pixels in the upper 95% of the distribution in $|B_z|$ (the criterion they used to determine the population they tracked), this can be seen in a number of statistical measures: the median horizontal field was five times stronger than the median vertical field; the mean and median inclination angles (from the vertical) were both larger than 65° ; and the emergence term in the Poynting flux was largest in every pixel above their tracking 5% threshold (and in 99% of all pixels).

Data from simulations by Bercik (2002) of a magnetic geometry similar to the plage region we study here have been obtained. He simulated magnetoconvection near the photosphere in the presence of a dynamically significant vertical magnetic field, with a detailed treatment of the energy equation. Tests using these data are planned, but a key challenge that must be addressed is the large disparity in temporal scales between the simulations and observations: in the

simulations by Bercik (2002), the characteristic time step is a second or less, but observational cadences are about a factor of 100 or more slower. Many of the velocities in the simulations are, in fact, very short-lived, and do not cause substantial magnetic evolution. Hence, direct comparison of instantaneous velocities in such simulations with velocities obtained by tracking (or other methods, e.g., Fisher et al. 2010, 2012) over an observationally realistic time interval Δt is problematic. Applying spatial and temporal averaging to the simulation data, however, might enable meaningful comparisons.

It is illuminating to compare the average Poynting flux that we obtain for our plage region with that obtained for the plage region studied by Yeates et al. (2014), both using FLCT flows: $2.20 \times 10^7 \text{ erg cm}^{-2} \text{ s}^{-1}$ and $1.30 \times 10^7 \text{ erg cm}^{-2} \text{ s}^{-1}$, respectively. Our flux is a factor of 1.7 larger than that reported by Yeates et al. (2014). We note that the mean and median unsigned vertical fields in our plage region (434 G and 354 G, resp.) are larger than the corresponding values in the region studied by Yeates et al. (2014) (365 G and 274 G, resp.) by factors of ~ 1.3 . We also used the SLCT flows to estimate the Poynting flux in the plage studied by Yeates et al. (2014) to be $1.73 \times 10^7 \text{ erg cm}^{-2} \text{ s}^{-1}$, about $\sim 30\%$ higher than the FLCT value. This substantial disparity suggests that uncertainties in Poynting estimate due to uncertainties in the flow estimates could be larger than the $\sim 15\%$ disparity that we found for the plage region that is the focus of this paper.

The occurrence of $S_z^{\text{plage,SLCT}} > S_z^{\text{plage,FLCT}}$ for both cases might be a coincidence, or might indicate that SLCT returns systematically higher Poynting flux estimates than FLCT. Further comparisons of flows and Poynting fluxes in additional regions would be useful to characterize systematic effects. In the case studied by Yeates et al. (2014), the SLCT and FLCT velocities and Poynting fluxes are again strongly correlated, with rank-order correlations for v_x, v_y , and S_z^{plage} of 0.75, 0.84, and 0.83, respectively.

3.2. Dependence on Magnetic Structure

The larger average Poynting flux from the plage region with larger area-averaged $|B_z|$ motivates analysis of the dependence of the Poynting flux on magnetic properties of each plage region. For both regions, rank-order correlations between $|S_z^{\text{plage}}|$ and the magnetic variables $|\mathbf{B}|, |\mathbf{B}_h|$, and $|B_z|$ are all similar, and very near 0.8. For spatial derivatives of magnetic variables, in both regions, the correlation of $|S_z^{\text{plage}}|$ with the horizontal curl $|\hat{\mathbf{z}} \cdot (\nabla_h \times \mathbf{B}_h)|$ ($\lesssim 0.2$) was slightly weaker than that with the horizontal divergence $|\nabla_h \cdot \mathbf{B}_h|$ (~ 0.3). For flow properties, in both regions the correlation of $|S_z^{\text{plage}}|$ and: $|\mathbf{v}_h|$ was weak ($\lesssim 0.2$); $|\hat{\mathbf{z}} \cdot (\nabla_h \times \mathbf{v}_h)|$ was negative and weak ($\gtrsim -0.2$); $(\nabla_h \cdot \mathbf{v}_h)$ was positive but weak enough to be insignificant; $|\nabla_h \cdot \mathbf{v}_h|$ was negative but weak.

These correlations of *unsigned* Poynting flux with field strengths suggest that stronger magnetic fields produce larger Poynting fluxes, which is perhaps unsurprising, given the product of field components in $|S_z^{\text{plage}}|$. To the extent that the presence of horizontal fields is correlated

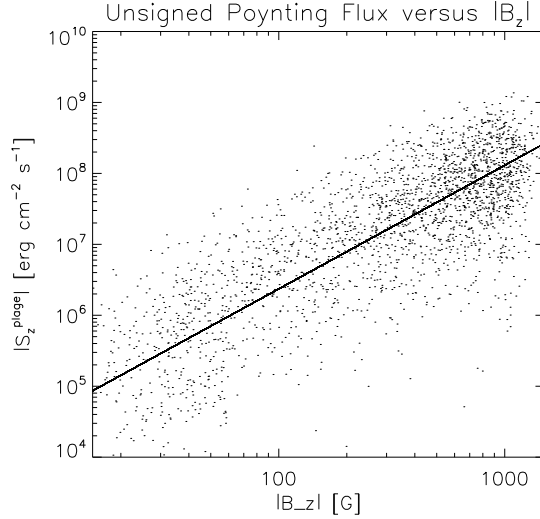


Fig. 6. A scatter plot of $|S_z^{\text{plage}}|$ versus $|B_z|$, and a least-squares linear fit to the logs, corresponding to a power law with $|S_z^{\text{plage}}| = 770|B_z|^{1.74}$. Given that the product of two magnetic field components enters the equation for the ideal Poynting flux, and that B_h is spatially correlated with B_z , a quadratic scaling is expected.

with the presence of vertical fields, this suggests an approximately quadratic scaling of $|S_z^{\text{plage}}|$ with $|B_z|$. In Figure 6, we show a scatter plot of $|S_z^{\text{plage}}|$ versus $|B_z|$, and a least-squares linear fit to the logs, corresponding to a power law with $|S_z^{\text{plage}}| = 770|B_z|^{1.74}$. This fit accords with our expectation of a near-quadratic dependence.

The dependence of the *signed* Poynting flux S_z^{plage} on $|\mathbf{B}|$, $|\mathbf{B}_h|$, and $|B_z|$ is much weaker, with rank-order correlations the range of 0.1 – 0.2 for both plage regions. For both regions, the correlation with $|\mathbf{B}_h|$ was slightly higher than with $|B_z|$, marginally beyond the $1 - \sigma$ level for each of the correlation coefficients (computed with Fisher’s z-transformation). A scatter plot (not shown) shows no clear trend, but a slight preponderance of positive Poynting fluxes is (barely) discernible.

In addition to the signed Poynting fluxes given above, we can characterize signed energy input per unit of magnetic flux, by computing a ratio with units of luminosity per maxwell of $|B_z|$. Among pixels that were tracked with FLCT, the mean ratios of signed energy input per maxwell are $3.6 \times 10^4 \text{ erg s}^{-1} \text{ Mx}^{-1}$ and $2.8 \times 10^4 \text{ erg s}^{-1} \text{ Mx}^{-1}$ for the plage region studied here and that studied by Yeates et al. (2014), respectively. As with differences in field strengths and signed Poynting fluxes between the plage regions, these differ by ~ 1.3 . The median (energy input:magnetic flux) ratios for tracked pixels in the respective regions are much smaller, and their ordering is reversed: $0.6 \times 10^4 \text{ erg s}^{-1} \text{ Mx}^{-1}$ and $1.1 \times 10^4 \text{ erg s}^{-1} \text{ Mx}^{-1}$. Totaling the energy input and unsigned magnetic flux separately, and then dividing — so the ratio of sums instead of the sum of ratios used to compute the mean above — yields $\sim 30\%$ larger values for the whole-FOV energy input per maxwell in both regions, $5.1 \times 10^4 \text{ erg s}^{-1} \text{ Mx}^{-1}$ and 3.6×10^4

erg s⁻¹ Mx⁻¹ for the plage region studied here and that studied by Yeates et al. (2014). (Again the regions differ by 1.3.) Cancellations within the sum of ratios used to compute the means above likely explain these larger whole-FOV values.

These (energy input:magnetic flux) ratios values are relevant to a study of soft-X-ray (SXR) luminosity L_x in several hundred active regions by Fisher et al. (1998), who investigated correlations between L_x and global magnetic properties of the regions (e.g., total unsigned flux, total unsigned vertical current, average field strength, etc.) from Haleakala Stokes Polarimeter vector magnetograms. They found that the regions' luminosities depended more strongly on their total unsigned magnetic flux, Φ , than any other global magnetic variable they considered, and, further, that L_x scaled as a power law in Φ , with an index near one. (See also Fludra and Ireland [2008], who investigated power laws between whole-AR EUV intensities and magnetic fluxes.) The lack of dependence on $|\mathbf{B}|$ reported by Fisher et al. (1998) is not consistent with the mean and whole-FOV energy input per unit magnetic flux that we find, which appear to scale with average field strength within the plage region. Given the difference between mean and median energy inputs per unit magnetic flux, this could be due to random fluctuations in a few high-Poynting-flux regions (which would bias the mean and whole-FOV values). Also, several unknown physical processes are at work in the conversion of magnetic energy into thermal energy and radiation (see, e.g., Klimchuk 2006), so disagreement between one component of energy input and one component of energy output is not especially problematic. In addition, given our uncertainties and our small sample (N of just 2!), additional regions must be studied to clarify the scaling of energy input with magnetic flux.

As we have seen, stronger-field pixels tend to have larger Poynting fluxes. The tendency of strong fields to inhibit convection (Title et al. 1992; Berger et al. 1998; Bercik 2002; Welsch et al. 2009; Welsch et al. 2012), however, also suggests that a turning point should be reached as field strength increases, where increasingly weak convective velocities produce a smaller convection-driven Poynting flux. This is a plausible explanation for the relative darkness of the corona in EUV and SXR images directly above sunspot umbrae. (Note, however, that spatially coherent, large-scale flows, like those in rotating sunspots [e.g., Brown et al. 2003], could still easily transport large amounts of magnetic energy across the photosphere in sunspot fields.) Do we see any evidence of this rollover in Poynting flux with field strength in our plage regions? To find out, we computed the average of signed Poynting fluxes in pixels above a set of increasing thresholds in field strength. Figure 7 shows signed Poynting fluxes S_z^{plage} averaged in pixels above a threshold in $|B_z|$, as functions of the threshold value, for our plage region (\triangle) and that studied by Yeates et al. (2014) (\times). The error bars show standard errors in the mean, and characterize variance in the Poynting flux more than observational uncertainties. While we do not observe a decrease in the average Poynting flux with increasing threshold, we do see a plateau in Poynting flux starting near 600 G, before fluctuations in the small number of above-threshold pixels (which have increasingly large unsigned Poynting fluxes) increase the

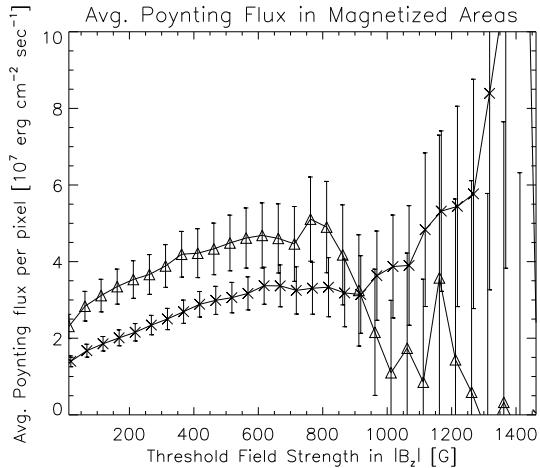


Fig. 7. Signed Poynting fluxes S_z^{plage} averaged in pixels above a threshold in $|B_z|$, as functions of the threshold value, for our plage region (\triangle) and that studied by Yeates et al. (2014) (\times). Values have been slightly offset horizontally to improve clarity. Error bars are standard errors in the mean, and characterize variance in the Poynting flux more than observational uncertainties. Intense magnetic fields should suppress convection, leading to a decrease in the convection-driven Poynting flux. While we do not observe a decrease in the average Poynting flux with increasing threshold, we do see a plateau in Poynting flux starting near 600 G, before fluctuations in the small number of above-threshold pixels increase the variance substantially.

variance substantially. Again, however, our uncertainties, small sample size, as well as our limited range of field strengths all preclude making definitive statements about the quenching of the convection-driven Poynting flux by strong fields.

3.3. Comparison with Chromospheric Emission

It is plausible that regions of enhanced magnetic energy flux across the photosphere would be brighter in some form of emission. (It is also possible that the solar atmosphere above the photosphere could store injected magnetic energy, in the form of electric currents, for some time prior to its dissipation and consequent enhancement of emission.)

The plage region we analyze here was also observed in Ca II by the BFI, so we briefly investigate correlations between the Poynting flux map and other photospheric magnetic variables and this emission. (The region studied by Yeates et al. 2014 was below the BFI FOV.) The closest image in time to the NFI velocity estimate was recorded at 20:30:16 UT on 2006/12/12, which we co-registered with B_{NFI} after downsampling from the BFI pixel size of $0.11''$ by a factor of three to approximately match the (2×2) -binned NFI pixel scale. In Figure 8, we show ± 125 and ± 250 Mx cm^{-2} contours of NFI flux density (solid for negative, dashed for positive) overlain on the Ca II intensity in a (100×100) -pixel area that encompasses our plage region.

For magnetic variables, the spatial map of Ca II intensity exhibited the strongest rank-order correlation (0.53) with $|B_z|$ and $|\mathbf{B}|$, and a weaker correlation (0.38) with $|\mathbf{B}_h|$.

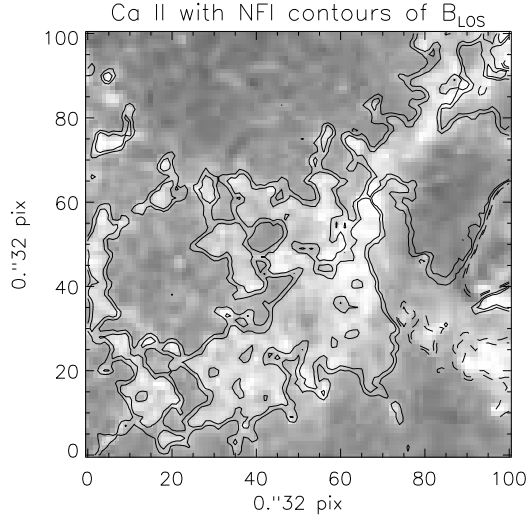


Fig. 8. ± 125 and ± 250 Mx cm^{-2} contours of NFI flux density (solid for negative, dashed for positive) are overlain on downsampled Ca II intensity from BFI in a (100×100) -pixel area that encompasses our plage region.

Correlations with the horizontal curl of \mathbf{B}_h , $|\hat{\mathbf{z}} \cdot (\nabla_h \times \mathbf{B}_h)|$, and its horizontal divergence, $|\nabla_h \cdot \mathbf{B}_h|$, were significant but much weaker, at 0.12 and 0.23, respectively.

For the Poynting flux, the correlation of Ca II intensity with unsigned and signed Poynting fluxes was 0.43, and 0.16, respectively. The fact that the magnetic variables that enter the Poynting flux are more strongly correlated with Ca II emission than the Poynting flux suggests that the only additional information in the Poynting flux, from the FLCT flows, is unrelated to Ca II emission; and, indeed, the correlation of Ca II with $|\mathbf{v}_h|$ is significantly negative, at -0.10. Correlations with the horizontal curl of \mathbf{v}_h , $|\hat{\mathbf{z}} \cdot (\nabla_h \times \mathbf{v}_h)|$, and its horizontal divergence, $|\nabla_h \cdot \mathbf{v}_h|$, were also negative, at -0.16 and -0.13, respectively. We also checked the *signed* horizontal flow divergence, reasoning that converging flows might slightly compress the plasma and lead to heating. The correlation was also negative (i.e., converging motions are present slightly more often near brighter Ca II emission), but weak, at -0.10. This might be related to the concentration of magnetic flux in downflow lanes where horizontal flows converge. The negative correlation of the curl, however, is harder to understand. We conclude that flow information at the spatial and temporal scales that we study has relatively little bearing on Ca II emission, compared to magnetic variables.

4. Summary & Conclusions

By combining LCT velocities estimated from a LOS magnetogram sequence with a vector magnetogram, both derived from *Hinode*/SOT observations of AR 10930, we estimated the ideal Poynting flux in a $(12 \text{ Mm} \times 12 \text{ Mm})$ plage region to be near $2.2 - 2.5 \times 10^7 \text{ erg cm}^{-2} \text{ s}^{-1}$, depending upon whether FLCT or SLCT velocities were used. Errors in the magnetic

fields likely produce smaller uncertainties in the Poynting flux than this. These Poynting fluxes are sufficient to explain the coronal energy demand estimated by Withbroe & Noyes (1977) ($\sim 1 \times 10^7$ erg cm $^{-2}$ s $^{-1}$), as well as a significant fraction of the chromospheric energy demand they estimated ($\sim 2 \times 10^7$ erg cm $^{-2}$ s $^{-1}$).

Our energy flux is larger by a factor of ~ 1.7 than that found in another plage region, observed by Yeates et al. (2014). The mean and median field strength in that region were lower by $\sim 30\%$ than the region we studied here, suggesting that signed Poynting flux might be higher in stronger-field regions. Within our plage region, we found that the *unsigned* Poynting flux from each pixel scaled as $\sim |B_z|^{1.7}$, i.e., nearly the quadratic scaling expected from the two components of \mathbf{B} that enter the expression for the ideal Poynting flux. The *signed* Poynting flux also increased with field strength, but with a much weaker correlation ($\lesssim 0.2$), so we could not easily quantify this trend. We found the energy input per unit magnetic flux in both plage regions to be on the order of $\sim 10^4$ erg s $^{-1}$ Mx $^{-1}$, with a tendency for the mean (but not median!) input to increase with average field strength in the plage region. Our uncertainties are large and our sample size is small, but this result conflicts with the study of X-ray luminosity versus magnetic field properties by (Fisher et al. 1998), who reported no dependence of magnetic field strength independent of the correlation with magnetic flux. We sought evidence that intense vertical fields might suppress convection and thereby limit the average signed Poynting flux from strong-field regions, but did not find clear evidence of this.

We also compared our Poynting flux map with a Ca II intensity image, and found much stronger correlation of Ca II emission with the vertical magnetic field strength $|B_z|$ than with vertical Poynting flux. We noted that the time interval Δt between images (eight minutes here) and windowing length scale L (4 pixels, ~ 1 Mm) used in our tracking will likely filter out processes on shorter temporal and spatial scales. Such processes (e.g., waves) might play a key role in Ca II emission. Given that chromospheric and coronal length scales are shorter than the scales we resolve, observations with higher resolution in space and time (see below) would be useful to investigate Poynting flux – emission correlations further.

We plan to conduct several related studies to extend the work here. We would like to analyze the same two plage regions with additional tracking methods (e.g., DAVE or DAVE4VM; Schuck 2006, Schuck 2008) to better understand the model-dependence of flow estimates in determining Poynting fluxes. We would also like to analyze additional *Hinode*/SOT datasets, especially observations with simultaneous IRIS (De Pontieu et al. 2014) coverage of chromospheric, transition region, and coronal emission, to seek any evidence of spatial or temporal correlations between energy input via our estimated Poynting fluxes and energy dissipation in the outer solar atmosphere. In addition, we would like to analyze a region simultaneously observed with *Hinode*/SOT and the HMI instrument aboard SDO (Scherrer et al. 2012), to study the dependence of the estimated Poynting flux on both instrument resolution (SOT’s is a factor of ~ 1.7 better) and combined spectral sampling / field inversion. Further, it is crucial

that we increase our sample size, and HMI's large database of active region patches (greater than 1,000 at the time of this writing) should be ideal for this purpose.

Within the larger context of the coronal heating problem, we suggest that a key strategic observational objective for understanding chromospheric and coronal heating should be construction of a detailed energy budget for the photosphere-to-corona system, with spatially and temporally resolved energy inputs correlated with energy release in all forms — radiation, kinetic energy in thermal and non-thermal particles and bulk motion, and gravitational potential energy. This will require high-resolution and high-cadence observations of the magnetic field and emission throughout the photosphere-to-corona system, for which both space-based observatories (e.g., SDO, IRIS, and the planned Solar-C satellite¹) and existing and planned ground-based observatories (NST [Goode et al.2010], GREGOR [Volkmer et al. 2010], ATST [Rimmele et al. 2010], and EST [Zuccarello and Zuccarello 2011]) will be essential.

Acknowledgements: We thank the *Hinode* science teams for their hard work in producing the excellent data that made this study possible. B.T.W. thanks A. Yeates for pursuing estimation of the Poynting flux in unipolar regions, which inspired this work. B.T.W. also thanks NWRA's K. D. Leka for help with SP data prepared by the late Tom Metcalf, and G.H. Fisher for providing useful comments about the manuscript that helped improve it. B.T.W. also gratefully thanks the Japan Society for the Promotion of Science, whose fellowship supported much of the work that underlies this study, and acknowledges funding from the NSF's National Space Weather Program under award AGS-1024862, the NASA Living-With-a-Star TR&T Program (grant NNX11AQ56G), and the NASA Heliophysics Theory Program (grant NNX11AJ65G). The authors are grateful to Japanese and U.S. taxpayers for providing the funds necessary to perform this work. *Hinode* is a Japanese mission developed and launched by ISAS/JAXA, collaborating with NAOJ as a domestic partner, and NASA and STFC (UK) as international partners. Scientific operation of the *Hinode* mission is conducted by the *Hinode* science team organized at ISAS/JAXA. This team mainly consists of scientists from institutes in the partner countries. Support for the post-launch operation is provided by JAXA and NAOJ (Japan), STFC (UK), NASA (USA), ESA, and NSC (Norway).

References

- Bercik, D. J. 2002, PhD thesis, Michigan State University
Berger, T. E., Loefdahl, M. G., Shine, R. S., & Title, A. M. 1998, ApJ, 495, 973
Bingert, S. & Peter, H. 2011, A&A, 530, A112
Brown, D. S., Nightingale, R. W., Alexander, D., Schrijver, C. J., Metcalf, T. R., Shine, R. A., Title, A. M., & Wolfson, C. J. 2003, Sol. Phys., 216, 79
Close, R. M., Parnell, C. E., Longcope, D. W., & Priest, E. R. 2004, ApJL, 612, L81

¹ <http://hinode.nao.ac.jp/SOLAR-C/Documents/Solar-C.e.pdf>

- Démoulin, P. & Berger, M. A. 2003, *Sol. Phys.*, 215, 203
- De Pontieu, B., Title, A. M., Lemen, J., Kushner, G. D., Akin, D. J., Allard, B., Berger, T., Boerner, P., Cheung, M., Chou, C., Drake, J. F., Duncan, D. W., Freeland, S., Heyman, G. F., Hoffman, C., Hurlburt, N. E., Lindgren, R. W., Mathur, D., Rehse, R., Sabolish, D., Seguin, R., Schrijver, C. J., Tarbell, T. D., Wuelser, J.-P., Wolfson, C. J., Yanari, C., Mudge, J., Nguyen-Phuc, N., Timmons, R., van Bezooijen, R., Weingrod, I., Brookner, R., Butcher, G., Dougherty, B., Eder, J., Knagenhjelm, V., Larsen, S., Mansir, D., Phan, L., Boyle, P., Cheimets, P. N., DeLuca, E. E., Golub, L., Gates, R., Hertz, E., McKillop, S., Park, S., Perry, T., Podgorski, W. A., Reeves, K., Saar, S., Testa, P., Tian, H., Weber, M., Dunn, C., Eccles, S., Jaeggli, S. A., Kankelborg, C. C., Mashburn, K., Pust, N., Springer, L., Carvalho, R., Kleint, L., Marmie, J., Mazmanian, E., Pereira, T. M. D., Sawyer, S., Strong, J., Worden, S. P., Carlsson, M., Hansteen, V. H., Leenaarts, J., Wiesmann, M., Aloise, J., Chu, K.-C., Bush, R. I., Scherrer, P. H., Brekke, P., Martinez-Sykora, J., Lites, B. W., McIntosh, S. W., Uitenbroek, H., Okamoto, T. J., Gummin, M. A., Auker, G., Jerram, P., Pool, P., & Waltham, N. 2014, ArXiv e-prints
- Fisher, G. H., Longcope, D. W., Metcalf, T. R., & Pevtsov, A. A. 1998, *ApJ*, 508, 885
- Fisher, G. H. & Welsch, B. T. 2008, in *Astronomical Society of the Pacific Conference Series*, Vol. 383, *Subsurface and Atmospheric Influences on Solar Activity*, ed. R. Howe, R. W. Komm, K. S. Balasubramaniam, & G. J. D. Petrie, 373–380; also arXiv:0712.4289
- Fisher, G. H., Welsch, B. T., & Abbett, W. P. 2012, *Sol. Phys.*, 277, 153
- Fisher, G. H., Welsch, B. T., Abbett, W. P., & Bercik, D. J. 2010, *ApJ*, 715, 242
- Fludra, A. & Ireland, J. 2008, *A&A*, 483, 609
- Galsgaard, K. & Nordlund, Å. 1996, *J. Geophys. Res.*, 101, 13445
- Goode, P. R., Coulter, R., Gorceix, N., Yurchyshyn, V., & Cao, W. 2010, *Astronomische Nachrichten*, 331, 620
- Gudiksen, B. V. & Nordlund, Å. 2002, *ApJ*, 572, L113
- Hagenaar, H., Schrijver, C., Title, A., & Shine, R. 1999, *ApJ*, 511, 932
- Hahn, M., Landi, E., & Savin, D. W. 2012, *ApJ*, 753, 36
- Ichimoto, K., Lites, B., Elmore, D., Suematsu, Y., Tsuneta, S., Katsukawa, Y., Shimizu, T., Shine, R., Tarbell, T., Title, A., Kiyohara, J., Shinoda, K., Card, G., Lecinski, A., Ständer, K., Nakagiri, M., Miyashita, M., Noguchi, M., Hoffmann, C., & Cruz, T. 2008, *Sol. Phys.*, 249, 233
- Isobe, H., Kubo, M., Minoshima, T., Ichimoto, K., Katsukawa, Y., Tarbell, T. D., Tsuneta, S., Berger, T. E., Lites, B., Nagata, S., Shimizu, T., Shine, R. A., Suematsu, Y., & Title, A. M. 2007, *PASJ*, 59, 807
- Klimchuk, J. A. 2006, *Sol. Phys.*, 234, 41
- Kosugi, T., Matsuzaki, K., Sakao, T., Shimizu, T., Sone, Y., Tachikawa, S., Hashimoto, T., Minesugi, K., Ohnishi, A., Yamada, T., Tsuneta, S., Hara, H., Ichimoto, K., Suematsu, Y., Shimojo, M., Watanabe, T., Shimada, S., Davis, J. M., Hill, L. D., Owens, J. K., Title, A. M., Culhane, J. L., Harra, L. K., Doschek, G. A., & Golub, L. 2007, *Sol. Phys.*, 243, 3
- Liu, Y. & Schuck, P. W. 2012, *ApJ*, 761, 105
- Meyer, K. A., Sabol, J., Mackay, D. H., & van Ballegooijen, A. A. 2013, *ApJL*, 770, L18
- Moon, Y.-J., Chae, J., Choe, G. S., Wang, H., Park, Y. D., Yun, H. S., Yurchyshyn, V., & Goode,

- P. R. 2002, *ApJ*, 574, 1066
- November, L. & Simon, G. 1988, *ApJ*, 333, 427
- Parker, E. N. 1983a, *ApJ*, 264, 635
- Parker, E. N. 1983b, *ApJ*, 264, 642
- Parker, E. N. 1984, *ApJ*, 280, 423
- Parker, E. N. 1988, *ApJ*, 330, 474
- Parnell, C. E. & De Moortel, I. 2012, *Royal Society of London Philosophical Transactions Series A*, 370, 3217
- Rappazzo, A. F., Velli, M., Einaudi, G., & Dahlburg, R. B. 2008, *ApJ*, 677, 1348
- Rimmele, T. R., Wagner, J., Keil, S., Elmore, D., Hubbard, R., Hansen, E., Warner, M., Jeffers, P., Phelps, L., Marshall, H., Goodrich, B., Richards, K., Hegwer, S., Kneale, R., & Ditsler, J. 2010, in *Society of Photo-Optical Instrumentation Engineers (SPIE) Conference Series*, Vol. 7733, *Society of Photo-Optical Instrumentation Engineers (SPIE) Conference Series*
- Scherrer, P. H., Schou, J., Bush, R. I., Kosovichev, A. G., Bogart, R. S., Hoeksema, J. T., Liu, Y., Duvall, T. L., Zhao, J., Title, A. M., Schrijver, C. J., Tarbell, T. D., & Tomczyk, S. 2012, *Sol. Phys.*, 275, 207
- Schrijver, C. J., De Rosa, M. L., Metcalf, T., Barnes, G., Lites, B., Tarbell, T., McTiernan, J., Valori, G., Wiegelmann, T., Wheatland, M. S., Amari, T., Aulanier, G., Démoulin, P., Fuhrmann, M., Kusano, K., Régnier, S., & Thalmann, J. K. 2008, *ApJ*, 675, 1637
- Schrijver, C. J., Title, A. M., Harvey, K. L., Sheeley, N. R., Wang, Y.-M., van den Oord, G. H. J., Shine, R. A., Tarbell, T. D., & Hurlburt, N. E. 1998, *Nature*, 394, 152
- Schuck, P. W. 2006, *ApJ*, 646, 1358
- . 2008, *ApJ*, 683, 1134
- Shimizu, T., Nagata, S., Tsuneta, S., Tarbell, T., Edwards, C., Shine, R., Hoffmann, C., Thomas, E., Sour, S., Rehse, R., Ito, O., Kashiwagi, Y., Tabata, M., Kodeki, K., Nagase, M., Matsuzaki, K., Kobayashi, K., Ichimoto, K., & Suematsu, Y. 2008, *Sol. Phys.*, 249, 221
- Suematsu, Y., Tsuneta, S., Ichimoto, K., Shimizu, T., Otsubo, M., Katsukawa, Y., Nakagiri, M., Noguchi, M., Tamura, T., Kato, Y., Hara, H., Kubo, M., Mikami, I., Saito, H., Matsushita, T., Kawaguchi, N., Nakaoji, T., Nagae, K., Shimada, S., Takeyama, N., & Yamamuro, T. 2008, *Sol. Phys.*, 249, 197
- Title, A. M., Topka, K. P., Tarbell, T. D., Schmidt, W., Balke, C., & Scharmer, G. 1992, *ApJ*, 393, 782
- Tomczyk, S., McIntosh, S. W., Keil, S. L., Judge, P. G., Schad, T., Seeley, D. H., & Edmondson, J. 2007, *Science*, 317, 1192
- Tsuneta, S., Ichimoto, K., Katsukawa, Y., Nagata, S., Otsubo, M., Shimizu, T., Suematsu, Y., Nakagiri, M., Noguchi, M., Tarbell, T., Title, A., Shine, R., Rosenberg, W., Hoffmann, C., Jurcevic, B., Kushner, G., Levay, M., Lites, B., Elmore, D., Matsushita, T., Kawaguchi, N., Saito, H., Mikami, I., Hill, L. D., & Owens, J. K. 2008, *Sol. Phys.*, 249, 167
- Volkmer, R., von der Lühe, O., Denker, C., Solanki, S. K., Balthasar, H., Berkefeld, T., Caligari, P., Collados, M., Fischer, A., Halbgewachs, C., Heidecke, F., Hofmann, A., Klvaňa, M., Kneer, F., Lagg, A., Popow, E., Schmidt, D., Schmidt, W., Sobotka, M., Soltau, D., & Strassmeier, K. G.

- 2010, *Astronomische Nachrichten*, 331, 624
- Welsch, B. T., Abbett, W. P., DeRosa, M. L., Fisher, G. H., Georgoulis, M. K. Kusano, K., Longcope, D. W., Ravindra, B., & Schuck, P. W. 2007, *ApJ*, 670, 1434
- Welsch, B. T., Christe, S., & McTiernan, J. M. 2011, *Sol. Phys.*, 274, 131
- Welsch, B. T., Fisher, G. H., Abbett, W. P., & Régnier, S. 2004, *ApJ*, 610, 1148
- Welsch, B. T., Kusano, K., Yamamoto, T. T., & Muglach, K. 2012, *ApJ*, 747, 130
- Welsch, B. T., Li, Y., Schuck, P. W., & Fisher, G. H. 2009, *ApJ*, 705, 821
- Withbroe, G. L. & Noyes, R. W. 1977, *ARA&A*, 15, 363
- Yeates, A. R., Bianchi, F., Welsch, B. T., & Bushby, P. J. 2014, *A&A*, submitted
- Zuccarello, F. & Zuccarello. 2011, in *IAU Symposium*, Vol. 274, *IAU Symposium*, ed. A. Bonanno, E. de Gouveia Dal Pino, & A. G. Kosovichev, 310–313